Computers & Geosciences 90 (2016) 64–77

Contents lists available at ScienceDirect

Computers & Geosciences

journal homepage: www.elsevier.com/locate/cageo

Case study

Improved triangular prism methods for fractal analysis of remotely sensed images

Yu Zhou [a,b], Tung Fung [a,c,*], Yee Leung [a,b]

[a] Department of Geography and Resource Management, The Chinese University of Hong Kong, Shatin, N.T., Hong Kong, PR China
[b] Institute of Future Cities, The Chinese University of Hong Kong, Shatin, N.T., Hong Kong, PR China
[c] Institute of Environment, Energy and Sustainability, The Chinese University of Hong Kong, Shatin, N.T., Hong Kong, PR China

ARTICLE INFO

Article history:
Received 23 February 2015
Received in revised form
11 February 2016
Accepted 26 February 2016
Available online 27 February 2016

Keywords:
Fractal dimension
Triangular prism method
Number of steps
Step sizes
Area of triangular prism facets

ABSTRACT

Feature extraction has been a major area of research in remote sensing, and fractal feature is a natural characterization of complex objects across scales. Extending on the modified triangular prism (MTP) method, we systematically discuss three factors closely related to the estimation of fractal dimensions of remotely sensed images. They are namely the (F1) number of steps, (F2) step size, and (F3) estimation accuracy of the facets' areas of the triangular prisms. Differing from the existing improved algorithms that separately consider these factors, we simultaneously take all factors to construct three new algorithms, namely the modification of the eight-pixel algorithm, the four corner and the moving-average MTP. Numerical experiments based on 4000 generated images show their superior performances over existing algorithms: our algorithms not only overcome the limitation of image size suffered by existing algorithms but also obtain similar average fractal dimension with smaller standard deviation, only 50% for images with high fractal dimensions. In the case of real-life application, our algorithms more likely obtain fractal dimensions within the theoretical range. Thus, the fractal nature uncovered by our algorithms is more reasonable in quantifying the complexity of remotely sensed images. Despite the similar performance of these three new algorithms, the moving-average MTP can mitigate the sensitivity of the MTP to noise and extreme values. Based on the numerical and real-life case study, we check the effect of the three factors, (F1)–(F3), and demonstrate that these three factors can be simultaneously considered for improving the performance of the MTP method.

1. Introduction

Feature extraction for land cover classification and change detection has been a major concern in remote sensing research (Townshend et al., 1991; Read and Lam, 2002; Ollier et al., 2003; Melgani and Bruzzone, 2004). In addition to pixel-based information, features reflecting spatial context of pixels have been considered important in the analysis of remotely sensed images in recent years (Lam, 2008). Fractal feature is a natural characterization of the texture of complex objects, particularly their self-similarity across scales (Mandelbrot, 1982). Theoretically, self-similarity means that the form of objects is invariant with respect to scales (Emerson et al., 1999). An ideal fractal object has no characteristic scale. However, the real-life geographical phenomena usually show different self-similarity properties at different scales, which was discussed by Emerson et al. (1999) as a multi-scale fractal feature. In addition, Emerson et al. (1999) showed that different landscapes exhibit different dependence of fractal features on the scales. Actually, the fractal features of many geographic phenomena, such as topography and urban landscapes in general and remotely sensed images in particular, have been discovered by Pentland (1984), Goodchild and Mark (1987), Lam and De Cola (1993), Batty and Longley (1994), and Gao and Xia (1996). Discussions on scale, resolution and fractal feature of geographical phenomena and processes have been made by Lam and Quattrochi (1992), Quattrochi et al. (1997), Xia and Clarke (1997), Emerson et al. (1999); papers in the 1994 special issue of the *International Journal of Remote Sensing* on 'Scaling in Remote Sensing', and the recent review by Sun et al. (2006).

Fractal dimension is an important concept that provides a rule to quantitatively measure the features of fractal objects (Feder, 1988). Because of its conceptual and computational simplicity, measure consistency and clarity, possession of a theoretical maximum and minimum, global and local computability, and applicability to classified and unclassified images, fractal dimension D_f is an important index for quantifying the complexity and roughness of images in many real-life studies (Lam, 2008). For a fractal object

* Corresponding author. Postal address: Department of Geography and Resource Management, The Chinese University of Hong Kong, Shatin, N.T., Hong Kong, PR China.
E-mail address: tungfung@cuhk.edu.hk (T. Fung).

http://dx.doi.org/10.1016/j.cageo.2016.02.018
0098-3004/

defined on a support with topological dimension D_t, the theoretical range of fractal dimension is $[D_t, D_t + 1]$ (Feder, 1988). With regard to a surface (D_t=2), its fractal dimension corresponds well to our intuitive notion of roughness and has a theoretical range from 2 to 3 (Pentland, 1984; Jaggi et al., 1993). The rougher surface has a larger value of fractal dimension. The extreme examples are a totally flat surface and an infinitely complex image whose fractal dimensions are 2 and 3, respectively (Jaggi et al., 1993; Qiu et al., 1999).

Fractal analysis has been applied to handle many problems in remote sensing. For example, Myint (2003) did some comparative studies between fractal features and some spatial indicators, such as autocorrelation and standard deviation; Hodgson (1998) paid attention to the effect of scales on image classification; Bretar et al. (2013) employed fractal dimension to characterize surface topography; Zhu et al. (2011) classified land-use/landcover types over a subtropical hilly region on the basis of fractal features; James et al. (2007) investigated the effects of DEM error on the study of fractal dimensions and scaling behaviors; Jiao et al. (2012) utilized fractal dimension as a shape metric for land-use classification or image-based land-use analysis; Liang et al. (2013) evaluated the effectiveness of fractal features for characterizing urban landscapes using multi-sensor satellite images; Shen et al. (2013) checked the correlation between corn progress stages and the fractal feature extracted from MODIS-NDVI time series; Cheng and Agterberg (2009) proposed a local singularity mapping technique which can be used to estimate the local fractal dimension of surfaces or maps. These studies have shown the important role fractals playing in feature extraction the different land use/land cover types, exemplified by vegetation types and urban landscapes. These features can be employed in the classification of remotely sensed problem and they have been shown to be superior to those obtained by the traditional methods. Such importance motivates the development of the fractal analysis of remote sensing data.

The ability of fractal dimension to extract features from remotely sensed images motivates many researchers to develop better estimation methods. The three most common methods are the triangular prism (TP) (Clarke, 1986), the variogram (Mark and Aronson, 1984) and the isarithm (Shelberg et al., 1983) methods. However, the original TP method tends to underestimate the fractal dimension (Jaggi et al., 1993), and a modified TP (MTP) method has been formulated and validated mathematically and experimentally (Lam et al., 2002; Zhao, 2001). Integrating the MTP and the other two methods, an image characterization and modeling system (ICAMS) has been developed for remote sensing analysis (Quattrochi et al., 1997). However, due to the difference in their estimation algorithms, the three methods may obtain different results for the same numerical experiment. Based on numerous comparisons, the MTP appears to be most reliable in analyzing complex remotely sensed images (Lam et al., 2002; Zhou and Lam, 2005). Even for images which may not be ideal fractals, the feature extracted by fractal analysis still can be treated as a fractal feature containing textural information of an image (Xia et al., 2010).

Despite its advantages, the MTP has been shown to be inaccurate in estimating the local surface area of the triangular prism facets (Sun, 2006) and incomplete in covering the triangular prisms on a surface (Ju and Lam, 2009a,b). It is thus necessary to have a more thorough examination of such estimation method. Because very little effort has been made on the systematic study of the algorithms of the MTP, we aim at the algorithmic investigation of the MTP and its improvement in this paper. As shown in more details in what follows, we systematically discuss the effects of the three factors on the estimation of fractal dimension, namely (F1) the number of steps; (F2) the step sizes; and (F3) estimation accuracy of the facet areas of the triangular prisms. Existing algorithms usually only focus on only one factor, such as (F2) in the divisor-step algorithm by Ju and Lam (2009a,b), and (F3) in the eight-pixel algorithm by Sun (2006). Taking into consideration all factors simultaneously, we propose three algorithms in the present study, namely the modification of the eight-pixel algorithm, the four-corner MTP and the moving-average MTP.

Although it is beyond the discussion in this study, we would like to point out another problem of the MTP for fractal analysis of remotely sensed images. It can be seen, from the implementation procedure of the MTP as we will describe in the following discussion, that the MTP can only be applied to a one-band imagery. For a multi-band imagery, it has to be transformed into some one-band images by using some data reduction methods, exemplified by the spectral indices (Ceccato et al., 2002), such as the NDVI (Lo, 1986; Jensen, 1986), the tasseled cap transformation (Kauth and Thomas, 1976), the principal component analysis (Munyati, 2004), and the rough set approach (Leung et al., 2013). An alternative way is to calculate the fractal dimension for each band so that a multi-band imagery can be studied via a spectrum consisting of fractal dimensions corresponding to each band (Qiu et al., 1999).

2. Materials and methods

2.1. Data

In this study, two types of data are employed, namely synthetic data and a real-life remotely sensed image.

The synthetic data are the fractional Brownian surface (FBS). FBS is a typical fractal surface, which has been widely employed to model the fractal process and to check the performance of algorithms in estimating fractal dimensions (Pentland, 1984; Zhao, 2001; Zhou and Lam, 2005; Sun, 2006; Emerson et al., 1999; Ju and Lam, 2009a,b). Given a position denoted by a two-dimensional vector $\vec{x}$, a function $I(\vec{x})$ can be called a FBS if for all $\vec{x}$ and increment $\Delta\vec{x}$, probability of $\left(\frac{I(\vec{x}+\Delta\vec{x})-I(\vec{x})}{\|\Delta\vec{x}\|^H} < y\right)$ equals $F(y)$, where H is known as the Hurst exponent and $F(y)$ is a cumulative distribution function (Pentland, 1984). For a FBS, H can be related to the corresponding fractal dimension D_f as $D_f = 3 - H$. Therefore, the FBS with smaller H corresponds to the larger D_f so that it is rougher. Fig. 1 visually illustrates this relationship using the FBS with H equals 0.2, 0.5 and 0.8 respectively.

Similar to the work by Silvetti and Delrieux (2013), we used two real-life examples to substantiate the application. One is a remote sensing image with size 250 × 250 pixels extracted from an IKONOS image of the Pearl River Delta, China. The bit depth and the spatial resolution of the IKONOS image are 11-bit and 4 m respectively. And the extracted image covers a typical residential landscape. The other is a nighttime light (NTL) image with the same size and covering the southeastern part of the USA. The NTL image is derived from the visible bands collected by the Defense Meteorological Satellite Program-Operational Line Scanner with annual visible band digital number (DN) of each pixel ranging from 0 to 63 and the spatial resolution of 1 km respectively. Comparing to the IKONOS image, the NTL image contains much less variation.

2.2. The TP and MTP method

In the following discussion, the size of a surface or an image is measured by the number of composing pixels. For simplicity, all surfaces considered are squares. As a matter of fact, the study using the fractal analysis can be extended to more irregular shapes (Schertzer and Lovejoy, 1987; Cheng, 2005). Because we usually pay attention to the square/rectangular remotely sensed images, in

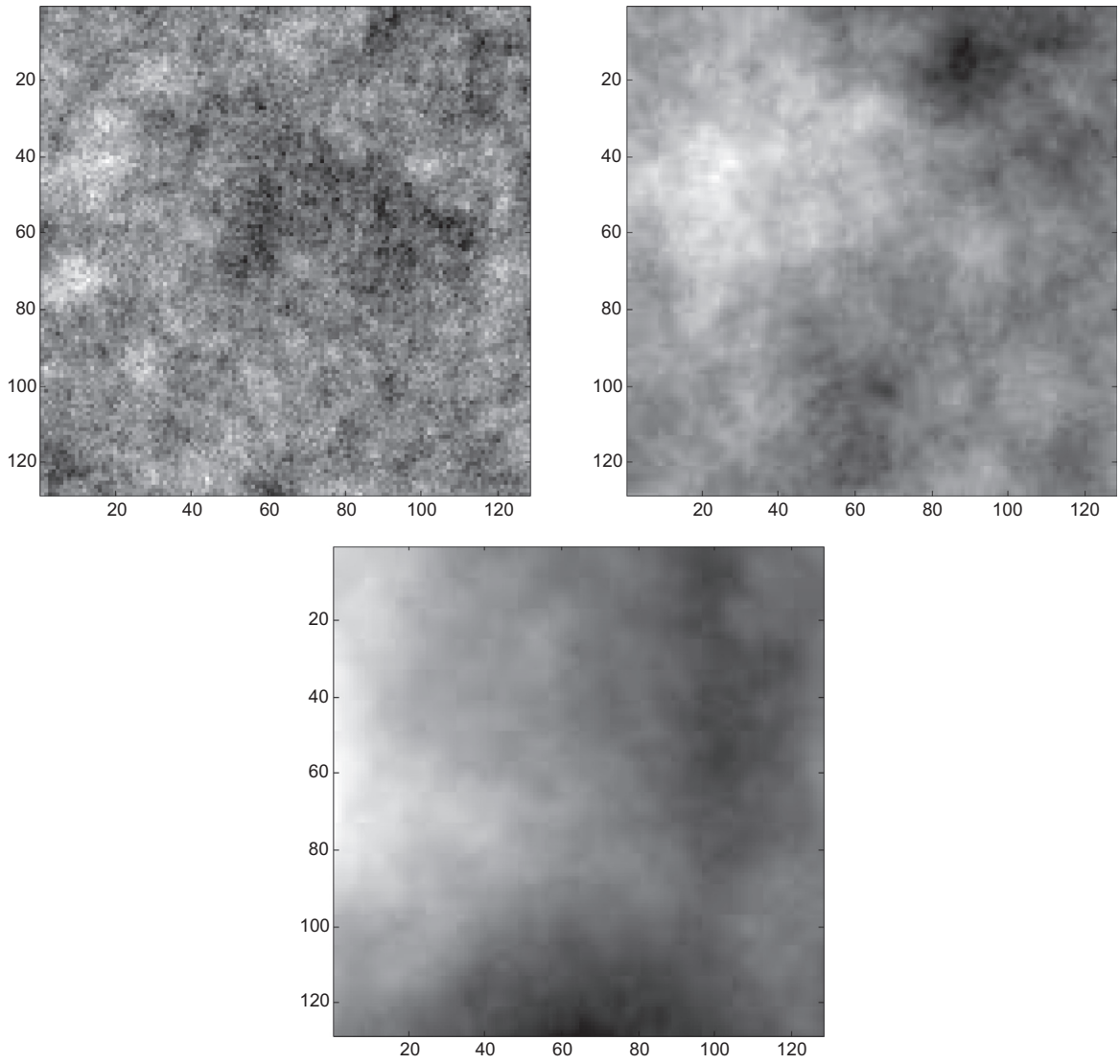

Fig. 1. Panels are arranged from the top left to the bottom as (a)–(c), corresponding to the FBS with Hurst exponent equaling 0.2, 0.5, and 0.8 respectively.

this work all studies focus on the square surface to facilitate discussion. These studies and discussions can be easily extended to the rectangular case.

The basic idea of the TP for estimating the fractal dimension of a surface of size $N \times N$ is as follows. First, for a given step size s, the surface is divided into non-overlapping subsurfaces of size $s \times s$. When s is not a divisor of $N-1$, part of the surface will be outside these subsurfaces. In general, it is known as the edge-effect problem in fractal analysis (Cheng, 2014). Some methods have been proposed to handle this problem, such as the gliding-box fractal analysis (Cheng, 1999). In a more specific way, we call it the incomplete coverage henceforth. Second, one triangular prism is constructed for each subsurface. The heights of the four corner vertices of the triangular prism are equal to the values of the surfaces of the corresponding four pixels. Their average constitutes the height of the central vertex. Third, the area of the subsurface can be estimated by the area of the prism facets consisting of four triangles formed by two adjacent corner vertices and the central vertex. Fig. 2(a and b) shows a 3D and top view of one triangular prism with step size s and height of four corner pixels and the central pixel a, b, c, d, and $e = \frac{a+b+c+d}{4}$. Then, this subsurface area for the step size s, $A(s)$, can be estimated by the summation of the four prism facets, e.g. $A_k(s)$ with $k=1, 2, 3, 4$ shown in Fig. 2(a). The fractal dimension D_f can be estimated via the power law $A(s) \sim (s^2)^{(2-D_f)}$ (Clarke, 1986). However, Zhao (2001) pointed out the inappropriate employment of the squared step size s^2 in the TP and proposed a modified TP (MTP) to estimate D_f via the relationship between $A(s)$ and s

$$A(s) \sim s^{(2-D_f)}. \tag{1}$$

Ju and Lam (2009a,b) claimed that the MTP is very robust in its estimation of the fractal dimension, and two factors, namely the number of steps and the step size, affect the estimation. Actually, the fractal dimension is estimated via the relationship between $A(s)$ and s (Eq. (1)), which is a straight line in the double-logarithmic plot if the power law exists. Fig. 2(c) gives an illustrative example of such relationship. It can be observed that the number of steps and the step size indeed affect the determination of the slope. If the number of steps is too small, then it will lead to statistically unreliable results. Given enough number of steps, if the step sizes are fixed at normal scales, they will become uneven (s with larger values becomes closer) at logarithmic scales, resulting in a biased estimation of the regression slope affected more likely by larger s and the corresponding $A(s)$. It is true that such biased estimation brings no impact on ideal fractals. However, in real life, images usually possess some noisy or non-fractal components. In this

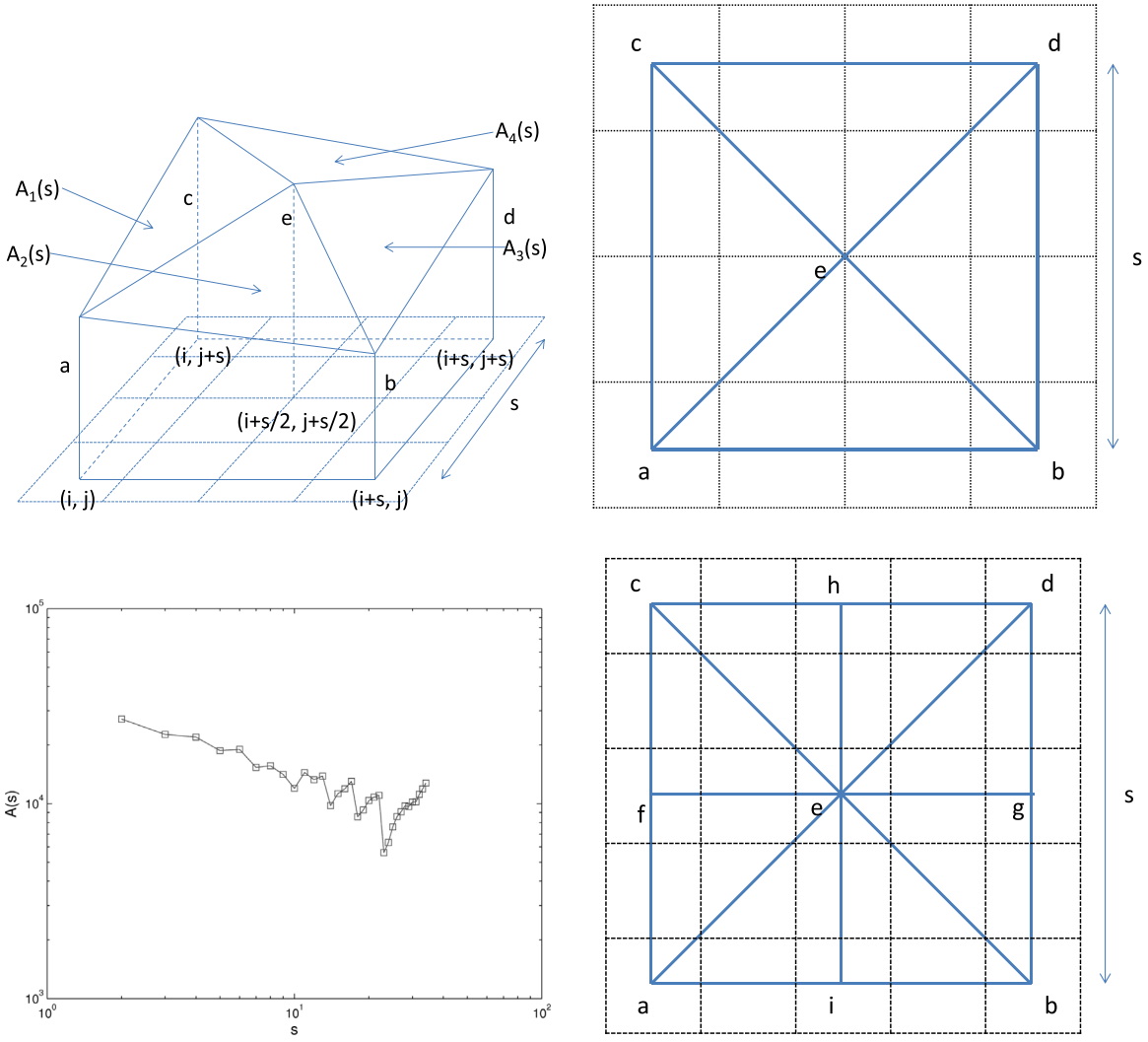

Fig. 2. Panels are arranged from the top left to the bottom right as (a)–(d). (a) A 3D view of one triangular prism with step size *s*. (b) A top view of one triangular prism with step size *s*, showing the corners employed in conventional algorithms of the TP and MTP method. (c) An illustrative example of the relationship between $A(s)$ and *s*. Here we employ the conventional MTP, which selects the step sizes as 1, 5, 9, …, 34. The analyzed surface is a FBS with size 69×69 and fractal dimension 2.4. (d) A top view of one triangular prism with step size *s*, showing the corners employed in the eight-pixel algorithm of the MTP method.

case, if we want to extract some features using fractal analysis in the concerned scaling range, an unbiased estimation of the slope can ensure us to obtain the averaged descriptors containing equal information at all scales. If the features at some specific scales are desired, we then just need to look into the behavior in a corresponding scaling range. Furthermore, it should also be noted that for large *s*, $A(s)$ may drop suddenly and then grows gradually (referring to Fig. 2(c)). Such behavior breaks the power law and makes negative impact on the slope estimation. This drop-and-grow behavior should come from the incomplete coverage of the constructed triangular prisms considered in Ju and Lam (2009a,b). It is reckoned that non-overlapping triangular prisms with some sizes, *s*, may not cover the whole surface. Introducing the coverage ratio R_c as the percentage of surface covered by constructed triangular prisms (Ju and Lam, 2009a,b), $A(s)$ corresponding to *s* having lower R_c should have less values.

Scrutinizing carefully the above procedure and Fig. 2(c), there should be an assumption behind the two factors suggested by Ju and Lam (2009a,b): "the values of each $A(s)$ should be accurate enough." However, as suggested by Sun (2006), the conventional way to estimate the area of the facet of a triangular prism covering each subsurface may introduce some errors. One of these errors is that the value *e* is calculated by averaging *a*, *b*, *c*, and *d* instead of by using the real height at the central pixel. The effect of this error might be very large for large *s*. Another one is the insufficiency of the employment of the four corners of the square subsurfaces.

Therefore, we have three factors that should be considered:

- (F1) the number of steps;
- (F2) the step size;
- (F3) estimation accuracy of the facets areas of the triangular prisms.

With respect to (F1), sufficient number of steps, actually the more the better, is needed to ensure estimation reliability. It is especially important if the surface is small. In terms of (F2), we have a twofold consideration. On one hand, step sizes should be even at logarithmic scales, i.e. the size should be increased by raising it to a certain power (Clarke, 1986). On the other hand, as suggested by Ju and Lam (2009a,b), step sizes have to be carefully selected to ensure that the constructed triangular prisms cover the whole surface, i.e. the sizes have to be divisors of $N-1$, here N is size of the surface. As a matter of fact, the number of steps has an upper limit, $N-1$. This upper limit corresponds to the smallest step size, i.e. one pixel. Therefore, our purpose is to select as many step sizes as possible from $[1, N-1]$ with two constraints: these

step sizes should be even at logarithmic scales and should overcome the incomplete coverage problem. With regard to (F3), Sun (2006) proposed the max-difference, mean-difference, and eight-pixel algorithms and showed the equivalence of the three algorithms. Referring to Fig. 2(d), the eight-pixel algorithm employs more corners compared with the conventional MTP so that the surface area of each triangular prism can be estimated by eight facets rather than four (Sun, 2006). Furthermore, Sun (2006) suggested the use of the actual height at the central pixel as e instead of computing it as the averaged height of other eight corners, i.e. a–d and e–i. Despite the above efforts made to improve the performance of the MTP, there are still some problems that need to be resolved. For example, there is insufficient number of steps for some N, e.g. only two usable divisors for $N=22$ and 23, and none for $N=24$. If the step sizes have to be increased by raising it to a certain power, then even a fewer number of steps can be selected, particularly for the estimation of the fractal dimensions for a small surface. Furthermore, these algorithms consider these three factors separately. The modifications made by Sun (2006) intend to solve problems of the third point but actually ignore problems caused by incomplete coverage. Because of the equivalence of the three algorithms proposed by Sun (2006), only the eight-pixel algorithm is considered in the following discussion.

2.3. Proposed MTP methods

To overcome the problem of incomplete coverage, the step sizes have to be carefully selected as the divisors of $N-1$. However, this selection method may significantly reduce the number of steps. Therefore, we need other ideas to handle the incomplete coverage problem. With these ideas, for factors (F1) and (F2) it is expected that we can use all step sizes $s \in [1, N-1]$ being even at logarithmic scales without other constraint. In addition, we employ the eight-pixel algorithm for factor (F3) because it should be a better estimate of the facets area of triangular prisms compared with the conventional MTP which employs only four corners.

In this subsection, we propose three algorithms accounting for all three factors simultaneously.

2.3.1. The modification of the eight-pixel algorithm

To give an approximation to the whole area when the constructed triangular prisms cannot completely cover the surface, a simple modification is to estimate the whole area of triangular prisms $A^*(s)$ as the area of the covered part $A(s)$ obtained by the eight-pixel algorithm divided by R_c. Here, R_c is the percentage of surface covered by the constructed triangular prisms (Ju and Lam, 2009a,b). In this sense, the fractal dimension D_f is estimated by the relationship $A^*(s) = A(s)/R_c \sim s^{(2-D_f)}$ instead of Eq. (1) directly.

This is a simple idea to handle the incomplete coverage. However, such modification is based on the assumption that a surface has similar properties for the covered part and the uncovered part. This assumption is true for some surfaces, e.g. remotely sensed images with single land cover/use, but it is invalid for some other surfaces, e.g. images with multiple land covers/uses. To overcome such weakness, we propose the following two algorithms.

2.3.2. The four-corner MTP

To avoid using the covered part to estimate the area of the uncovered part, we develop the four-corner MTP. The basic idea of this algorithm is illustrated in Fig. 3. In this example, the size of the surface is $N \times N$ with $N=11$ and the four corners of this surface are marked as A, B, C, and D. For illustration, we use step size $s=4$. The procedure can be easily extended to other N and s. First, the triangular prisms are constructed to start the cover from corner A,

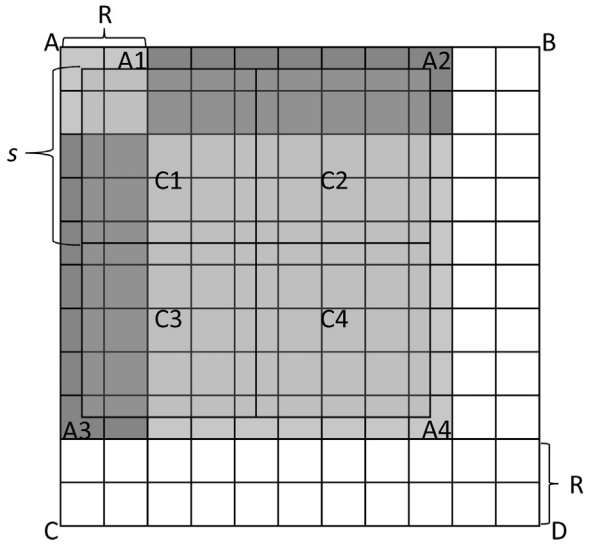

Fig. 3. An illustrative description to show the procedure of the four-corner MTP. Here the size of the studied surface N is 11, and the size of the covering triangular prism s is 4.

only four triangular prisms C1, C2, C3, and C4 are constructed. Similar cover can be constructed from the other three corners, namely B, C, and D. Second, we denote the covers starting from the four corners by the same symbols A, B, C, and D respectively and divide cover A into four parts A1, A2, A3, and A4, depending on how they are covered by A, B, C, and D. It can be observed that A1 can only be covered by the cover A, A2 and A3 by both cover A and cover B, while A4 by all four covers. Then, the contribution of cover A to the whole surface area should be $\mathrm{A1} + \frac{\mathrm{A2}+\mathrm{A3}}{2} + \frac{\mathrm{A4}}{4}$. Denoting the size of A1 as $R \times R$ with $R = N - 1 - s$, the areas of A1, A2, A3, and A4 can then be estimated as follows: $\mathrm{A1} = \mathrm{C1}\frac{R^2}{s^2}$, $\mathrm{A2} = (\mathrm{C1}+\mathrm{C2})\frac{R}{s} - \mathrm{A1}$, $\mathrm{A3} = (\mathrm{C1}+\mathrm{C3})\frac{R}{s} - \mathrm{A1}$, and A4=A–A1–A2–A3. Similarly, the contribution of covers B, C, and D can also be computed. Therefore, the whole of the surface area for step size $s=4$ can be estimated as $A^*(s) = \mathrm{A} + \mathrm{B} + \mathrm{C} + \mathrm{D}$. D_f then can be estimated by $A^*(s) \sim s^{(2-D_f)}$.

2.3.3. The moving-average MTP

Inspired by the idea of the gliding box employed in the improvement of other fractal analyses (Cheng, 1999), we employ the moving triangular prism with overlappings to ensure a complete coverage. Moving the triangular prism by one pixel once, we can ensure that the surface is covered by at least one triangular prism no matter how the step size s is selected. Then the area contributed by each pixel (i,j) is determined by $\{\tilde{A}_{k_{i,j}}(s)\}$ with $k_{i,j} = 1, \ldots, w_{i,j}$, where $\{\tilde{A}_{k_{i,j}}(s)\}$ are the areas of the triangular prisms covering the pixel (i,j) and $w_{i,j}$ is the number of these triangular prisms which can be represented as follows:

- for $j \le s+1$:

$$w_{i,j} = \begin{cases} i \cdot j, & \text{if } i \le s \\ (s+1) \cdot j, & \text{if } s < i \le N-s; \\ (N-i+1) \cdot j, & \text{if } i > N-s \end{cases}$$

- for $s+1 < j \le N-s$:

$$w_{i,j} = \begin{cases} i \cdot (s+1), & \text{if } i \le s \\ (s+1)^2, & \text{if } s < i \le N-s; \\ (N-i+1) \cdot (s+1), & \text{if } i > N-s \end{cases}$$

- for $j > N-s$:

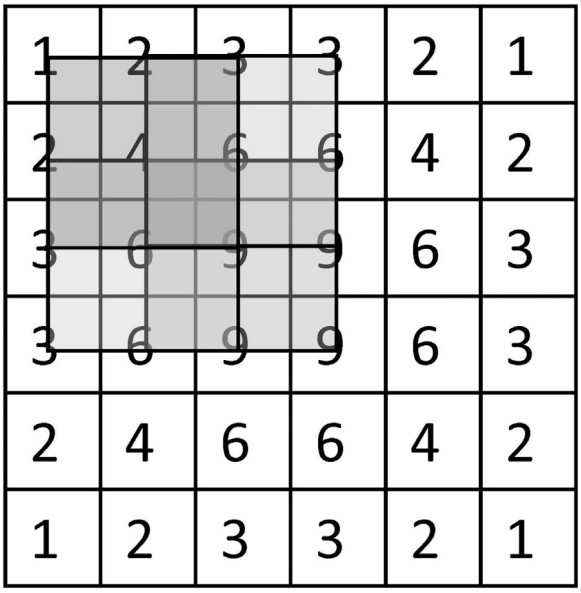

Fig. 4. An illustration showing the way the triangular prism is moved to cover the surface and the number (expressed as the number in this figure) of triangular prisms covering each pixel. Here the size of surface N is 6, the step size of the covering triangular prism s is 2.

$$w_{i,j} = \begin{cases} i\cdot(N-j+1), & \text{if } i \le s \\ (s+1)\cdot(N-j+1), & \text{if } s < i \le N-s. \\ (N-i+1)\cdot(N-j+1), & \text{if } i > N-s \end{cases}$$

Denote , then $A^*(s) = \sum_{i,j=1}^{N-1} \frac{1}{w_{i,j}s^2} \sum_{k_{i,j}=1}^{w_{i,j}} \tilde{A}_{k_{i,j}}(s)$. To facilitate the understanding of this algorithm, we give a visual example in Fig. 4 by taking the surface size $N=6$ and step size $s=2$. By checking the relation $A^*(s) \sim s^{(2-D_f)}$, D_f can be computed.

3. Calculation

For the synthetic data, the experimental design is the same as that of Ju and Lam (2009a,b), except for the additional consideration of sizes 129×129 and 257×257. Similar to Sun (2006) and Ju and Lam (2009a,b), performances of the algorithms are evaluated by the mean of the computed fractal dimensions and their root mean squared error (RMSE) relative to the expected values.

With regard to the extracted remotely sensed image, the proposed algorithms and the divisor-step algorithm, as a comparison, are applied to compute the local fractal dimensions. Here, the concept of local fractal dimension is similar to that employed by De Jong and Burrough (1995). We introduce a local kernel that moves vertically/horizontally just one pixel once of the extracted image and then estimate the local fractal dimension of the part of the image in this kernel. The size of the moving kernel ranges from 9×9 to 69×69 with a step 4. After obtaining the fractal dimension in the moving kernel, a fractal layer can be composed. Actually, it is impossible to obtain a fractal dimension for just one pixel but for an image or sub-image. Here one local fractal dimension can be estimated for the moving kernel at each position. Therefore, the fractal layer has the large spatial resolution. To provide a benchmark for comparison by observation at the same spatial resolution, we also resample the image using the same moving kernel. We calculate the local average in the kernel as the resampled value. In addition, we check the dependence of the computed local fractal dimension on the moving-kernel size. For each algorithm, we calculate the mean of the computed fractal dimensions in the moving kernel for each of the 16 sizes (from 9×9 to 69×69). Furthermore, we calculate the mean values, the corresponding standard deviations, extremes and the ranges for the local fractal dimensions obtained by each algorithm. For the NTL example, we calculate the local fractal layer using the moving kernel with size 21×21 and 23×23 for comparison.

4. Results and discussion

4.1. Synthetic data

Here, the divisor-step, modification of the eight-pixel, four-corner, and moving average algorithm are marked by the algorithms I, II, III, and IV, and they are applied to the simulated FBSs. We present the results in Figs. 5, 7 and 8. In all these figures, the horizontal lines in the upper panels indicate the expected value of the fractal dimensions. Thus, the closer to the corresponding line, the better the performance achieved by the algorithm. In the bottom panel, the smaller the RMSE, the better of the algorithm performs.

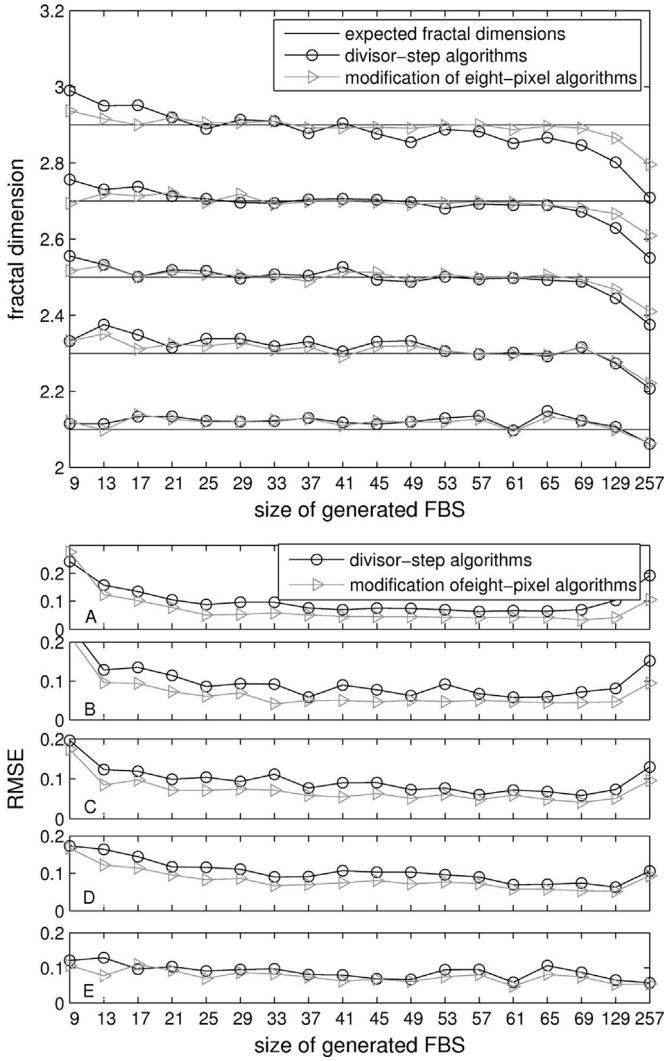

Fig. 5. The comparison of the mean of computed fractal dimensions (the upper panel) and the RMSE (the bottom panel) obtained by the divisor-step algorithm and the modification of the eight-pixel algorithm. Subpanels (A)–(E) of the bottom panel correspond to fractal dimensions 2.9, 2.7, 2.5, 2.3, and 2.1 respectively.

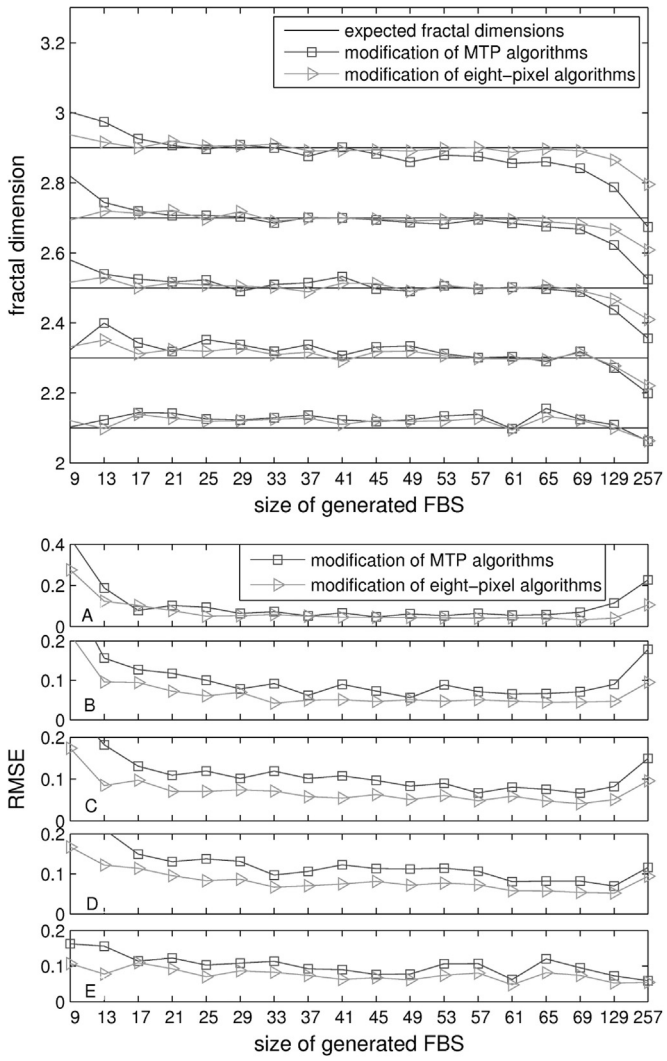

Fig. 6. The comparison of the mean of computed fractal dimensions (the upper panel) and the RMSE (the bottom panel) obtained by the modification of the MTP and the modification of the eight-pixel algorithm. Subpanels (A)–(E) of the bottom panel correspond to fractal dimensions 2.9, 2.7, 2.5, 2.3, and 2.1 respectively.

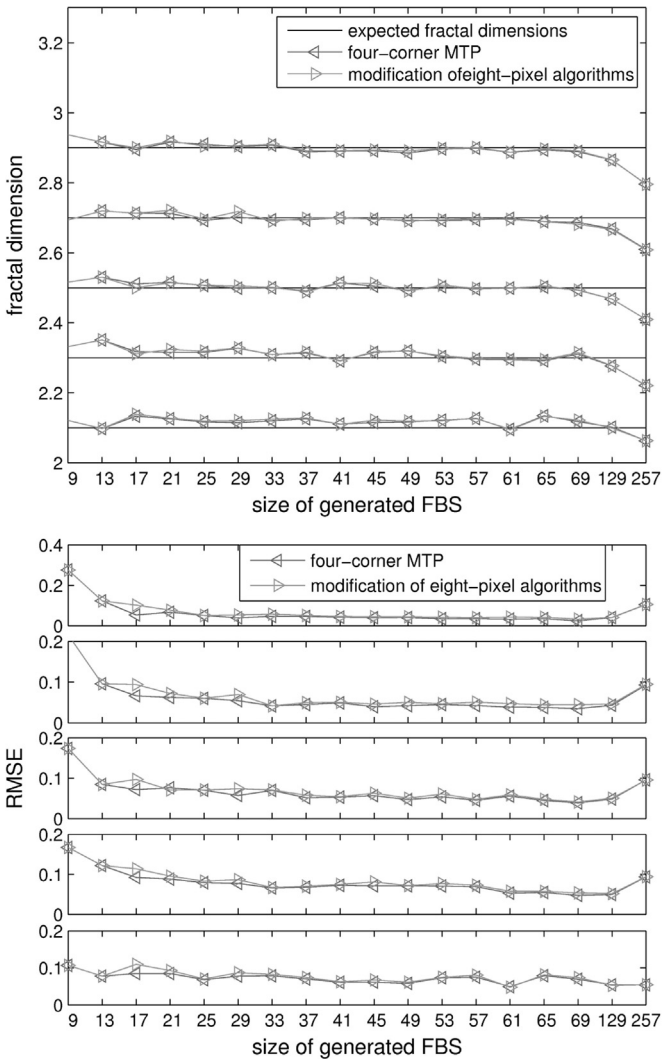

Fig. 7. The comparison of the mean of computed fractal dimensions (the upper panel) and the RMSE (the bottom panel) obtained by the four-corner and modification of eight-pixel algorithm.

It can be observed from Fig. 5 that with regard to both the mean of the computed fractal dimensions and the RMSE, algorithm II works better than algorithm I for all simulated FBSs. In particular, such superiority obviously appears in FBSs with large fractal dimensions and/or large sizes. It is because, in general, the larger the fractal dimension, the more complex the surface. In addition, it is more likely to have large variations on surface with large size. For a subsurface covered by a constructed triangular prism, eight triangles employed by algorithm II should fit the real situation, better than the four triangles in algorithm I, especially for surfaces of higher complexity and variability.

One may argue that the superiority of algorithm II is due to the different selections of the step size. To check the effect of the step size selection, we give a modification of algorithm I by using geometric-step sizes. The way for estimating the whole area is the same as that in algorithm II under incomplete coverage. The comparison presented in Fig. 6 confirms the superiority of algorithm II.

Fig. 7 shows that performance of the algorithm III is at least comparable to that of algorithm II, but it is even better for some step sizes, e.g. $s=17$, 29. Fig. 8 depicts the comparison of algorithms III and IV. No significant difference can be found between them from either the mean of the computed fractal dimensions or the RMSE.

To give a more quantitative comparison of algorithms I–IV, we calculate the averaged values of the computed fractal dimensions and the RMSE for all 18 different step sizes for each algorithm. The numerical results are listed in Table 1. The mean values of fractal dimensions are similar. However, the divisor-step algorithm results in larger RMSE. It should also be emphasized that the divisor-step algorithm just works for the surface with specific size, but our proposed algorithms are free from such limitation.

Fig. 9 shows the relationship between $A(s)$ and s obtained by algorithm II using the same FBS employed in Fig. 2(c). Compared with the relationship obtained by the conventional MTP, this relationship has been significantly improved, exhibiting a very good power-law for the estimation of the fractal dimension.

Although the performance of the MTP algorithm has been improved, some problems still remain. They are related to factor F1. Results obtained by the proposed algorithms depicted in Figs. 5, 7 and 8 show that for surfaces with large sizes, i.e. 129×129 and 257×257, all algorithms underestimate the fractal dimension and the RMSE is large, particularly for surfaces with large fractal dimensions ($D_f=2.7$, 2.9). It can be attributed to greater variations in larger surfaces, and higher surface complexity due to larger fractal dimensions. Therefore, it is more difficult to accurately estimate the area. However, the proposed algorithms perform much better than the divisor-step algorithm for large

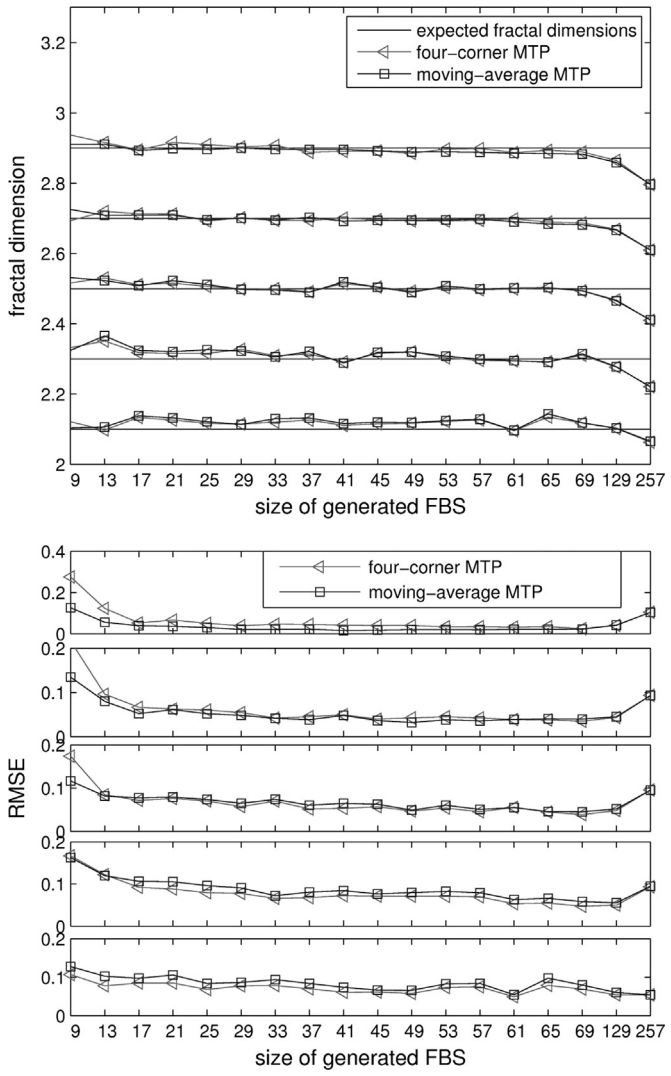

Fig. 8. The comparison of the mean of computed fractal dimensions (the upper panel) and the RMSE (the bottom panel) obtained by the four-corner and moving-average algorithm.

surfaces. With regard to surfaces with small sizes, the computed fractal dimension seems to be fine, but the RMSE is greater than those of moderate sizes. Such phenomenon should be due to the fact that the computed fractal dimension is unstable because the number of usable step sizes is small. As a conclusion, the proposed algorithms are able to obtain reliable results for the moderate sizes, e.g. from 17×17 to 69×69, of all fractal dimensions. With regard to the surface with smaller or larger sizes, the results become less accurate, especially for simulated FBMs with fractal dimension larger than 2.5.

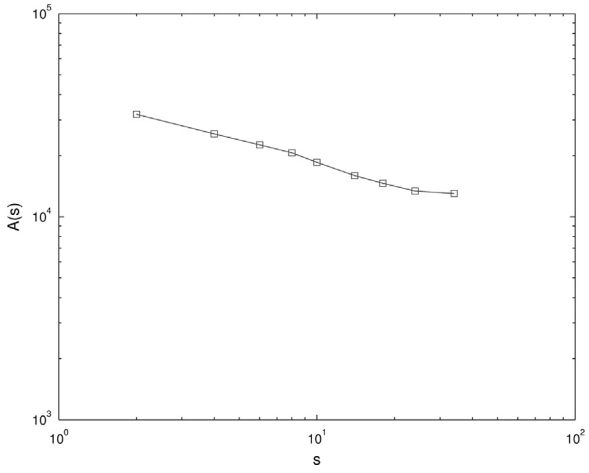

Fig. 9. An illustrative example of the relationship between $A(s)$ and s. Here we employ the four-corner MTP. The analyzed surface is a FBS with size 69×69 and fractal dimension 2.4.

4.2. Real-life remotely sensed image

The effectiveness of algorithms I–IV in analysis of the real-life image is discussed in this subsection.

The original image, the resampled image and the visualized fractal layers obtained by algorithms I–IV for step size $s=21$ are depicted in Fig. 10. To visually compare results on the same basis, all images are rescaled to 0–255 for display. Fractal layers obtained by algorithms I–IV correspond to panels (c)–(f) in Fig. 10. As a whole, fractal layers can generally reflect the basic texture information of the image shown in panel (a). In particular, referring to the resampled image in panel (b), obvious features such as the road running vertically across the image about one-third from the right and some house roofs appearing as white lumps can find good correspondence at fractal layers: the edge of the road is white with large fractal dimensions indicative of strong variations, but the roofs black lumps suggest their smoothness and flatness. To see fractal layers separately, the fractal layer (panel (c)) obtained by the divisor-step algorithm is brighter than the others, indicating higher fractal dimensions than those of the others. The modified eight-pixel algorithm and the four-corner algorithm result in the similar fractal layers (panel (d) and (e) respectively). Many black points can be detected in panels (c)–(e), which might be caused by the sensitivity of the MTP to the noise or extreme grey level values (Qiu et al., 1999; Sun et al., 2006), the cars parking on the road or the blinks on the roofs as extreme values in here. Visually, the fractal layer in panel (f) seems to be blurrier than the other fractal layers. These different effects may be attributed to the moving-average procedure of the algorithm, which mitigates the sensitivity. Compared to the resampled image in panel (b), such blurring, however, makes the basic features more obvious in the fractal layers. Furthermore, it should be emphasized that more information can be observed from the fractal layers than the resampled image. For example, the road which is obvious in

Table 1
The averaged fractal dimensions respectively obtained by algorithms I, II, III, and IV, corresponding to the divisor-step, modified eight-pixel, four-corner, moving-average algorithm, and their RMSE for all 18 step sizes (from 9×9 to 69×69 as well as 129×129 and 257×257). The expected values are also listed for reference.

Algorithms	Computed fractal dimensions					RMSE				
(Expected values)	2.90	2.70	2.50	2.30	2.10	0	0	0	0	0
I	2.88	2.69	2.50	2.31	2.12	0.10	0.10	0.10	0.10	0.09
II	2.89	2.69	2.50	2.31	2.12	0.07	0.07	0.07	0.08	0.08
III	2.89	2.69	2.50	2.31	2.11	0.06	0.06	0.07	0.08	0.07
IV	2.89	2.69	2.50	2.31	2.12	0.04	0.05	0.07	0.09	0.08

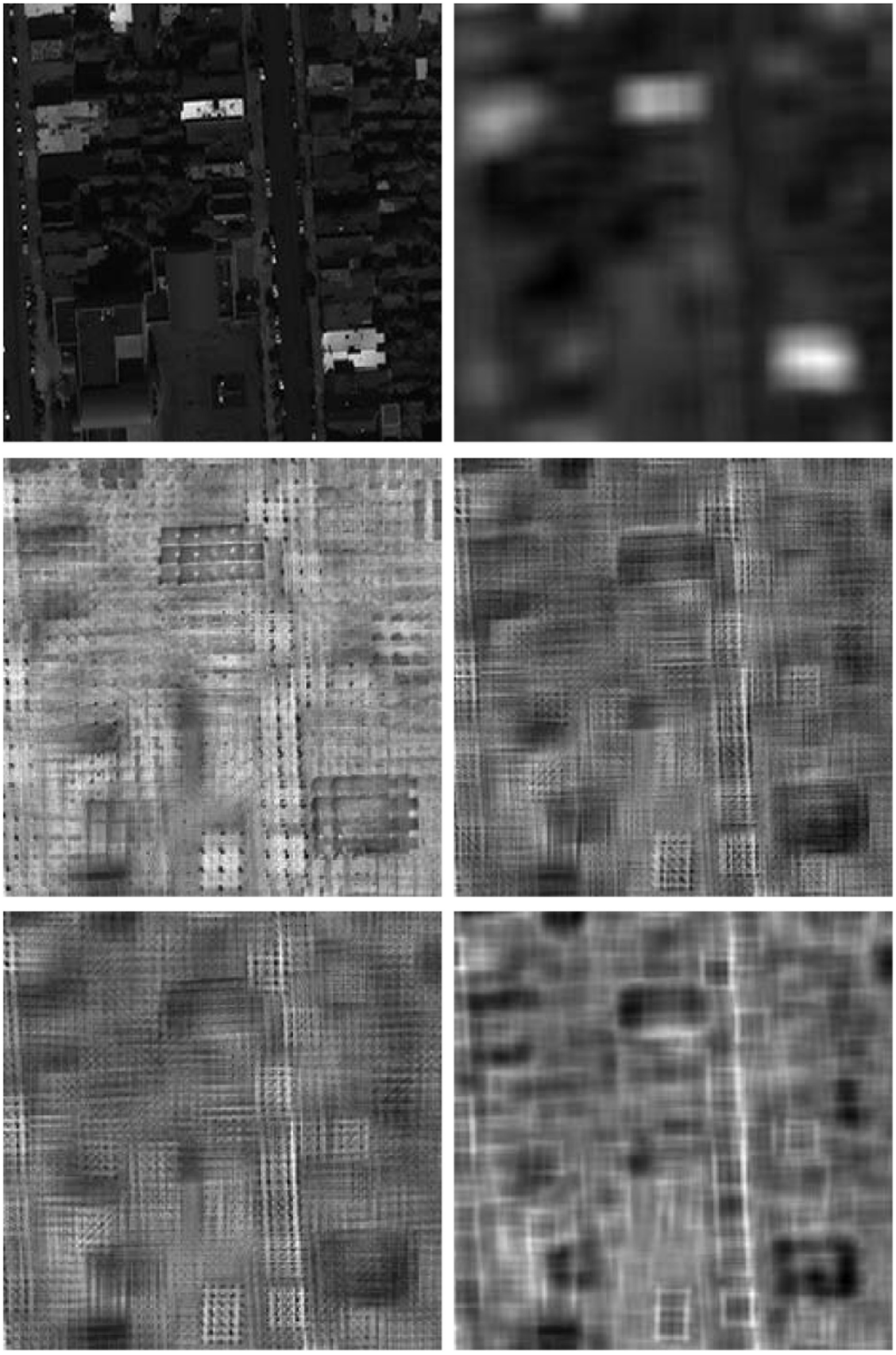

Fig. 10. Panels are arranged from the top left to the bottom right as (a)–(f). (a) The image extracted from an IKONOS image covering a typical residential land cover. (b) Resampled image of the image in panel (a) using overlapping moving kernel with size 21×21. Panels (c)–(f) are fractal layers obtained for moving kernel with size 21×21 by the divisor-step algorithm, the modified eight-pixel algorithm, the four-corner algorithm and the moving-average algorithm, respectively. The images displayed in all panels are rescaled to 0–255 for visual comparison.

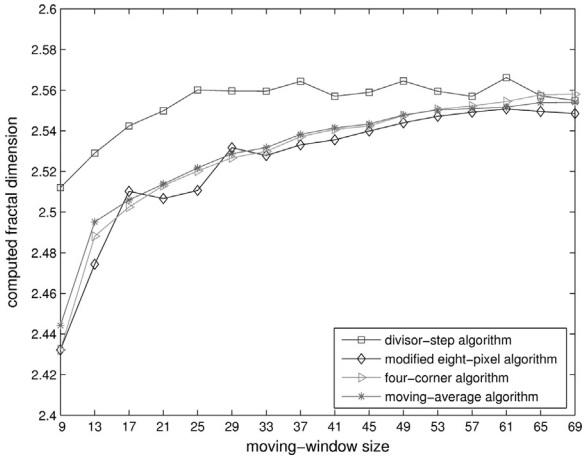

Fig. 11. The averaged values of the estimated fractal dimensions using the divisor-step algorithm and our proposed algorithms.

Table 2
Averaged value of the computed local fractal dimensions and standard deviations (SD) of the extracted IKONOS residential image for each of the 16 moving-kernel sizes (from 9×9 to 69×69) for algorithms I, II, III, and IV, corresponding to the divisor-step, modified eight-pixel, four-corner, and moving-average algorithms respectively.

Sizes	Computed fractal dimensions ($\pm$SD)			
	Algorithm I	Algorithm II	Algorithm III	Algorithm IV
9×9	2.51 ($\pm$0.23)	2.43 ($\pm$0.22)	2.43 ($\pm$0.22)	2.44 ($\pm$0.18)
13×13	2.53 ($\pm$0.18)	2.47 ($\pm$0.15)	2.49 ($\pm$0.17)	2.50 ($\pm$0.15)
17×17	2.54 ($\pm$0.17)	2.51 ($\pm$0.18)	2.50 ($\pm$0.14)	2.51 ($\pm$0.13)
21×21	2.55 ($\pm$0.14)	2.51 ($\pm$0.12)	2.51 ($\pm$0.12)	2.51 ($\pm$0.11)
25×25	2.56 ($\pm$0.12)	2.51 ($\pm$0.10)	2.52 ($\pm$0.11)	2.52 ($\pm$0.10)
29×29	2.56 ($\pm$0.12)	2.53 ($\pm$0.11)	2.53 ($\pm$0.10)	2.53 ($\pm$0.09)
33×33	2.56 ($\pm$0.11)	2.53 ($\pm$0.10)	2.53 ($\pm$0.09)	2.53 ($\pm$0.08)
37×37	2.56 ($\pm$0.10)	2.53 ($\pm$0.09)	2.54 ($\pm$0.08)	2.54 ($\pm$0.08)
41×41	2.56 ($\pm$0.09)	2.54 ($\pm$0.08)	2.54 ($\pm$0.08)	2.54 ($\pm$0.07)
45×45	2.56 ($\pm$0.09)	2.54 ($\pm$0.09)	2.54 ($\pm$0.07)	2.54 ($\pm$0.07)
49×49	2.56 ($\pm$0.08)	2.54 ($\pm$0.08)	2.55 ($\pm$0.07)	2.55 ($\pm$0.07)
53×53	2.56 ($\pm$0.09)	2.55 ($\pm$0.08)	2.55 ($\pm$0.07)	2.55 ($\pm$0.06)
57×57	2.56 ($\pm$0.08)	2.55 ($\pm$0.07)	2.55 ($\pm$0.07)	2.55 ($\pm$0.06)
61×61	2.57 ($\pm$0.07)	2.55 ($\pm$0.07)	2.55 ($\pm$0.06)	2.55 ($\pm$0.06)
65×65	2.56 ($\pm$0.08)	2.55 ($\pm$0.07)	2.56 ($\pm$0.06)	2.55 ($\pm$0.06)
69×69	2.55 ($\pm$0.08)	2.55 ($\pm$0.07)	2.56 ($\pm$0.06)	2.55 ($\pm$0.05)

the original image shown in panel (a) becomes obscure in panel (b). However, it is still observable in panels (c)–(e), especially in panels (d)–(e). It means that the fractal layers can also retain the detailed information at the original resolution in panel (a), in addition to the information in the moving kernel shown in panel (b).

To check dependence of local fractal dimensions on the kernel size, we calculate the mean values for each size and plot against the corresponding size in Fig. 11. The calculated values are plotted against the kernel sizes (Fig. 11). The mean values obtained by the divisor-step algorithm are larger and with greater fluctuation than those obtained by algorithms II–IV for kernel size no more than 61×61. As to sizes 65×65 and 69×69, four algorithms give similar values. With regard to algorithms II–IV, their mean values are very close to one another for all kernel sizes. However, it should be noted that a little bit more fluctuation at the sizes 17×17 and 29×29 can be found in the results obtained by algorithm II.

The mean values and the corresponding standard deviations are listed in Table 2. For all kernel sizes, algorithms II–IV have smaller deviations than algorithm I, in particular the moving-average MTP reaches the minimum deviation. In addition, for all four algorithms, their computed fractal dimensions also grow while the standard deviations become smaller with the increase of the moving-kernel size. Such pattern indicates that, among all four algorithms, algorithm I is most sensitive to variations while algorithm IV is most robust.

As mentioned, the fractal dimension of a surface should be between 2 and 3. Thus, we list the extremes and their ranges obtained by each of the four algorithms for each of the 16 moving-kernel sizes in Table 3. The extremes obtained by algorithm I are outside the theoretical range for kernel sizes less than 37×37, with the maximum computed fractal dimensions getting to be even larger than 4. On the other hand, our proposed algorithms give local fractal dimensions within the theoretical ranges for sizes larger than 21×21, except for a value equaling 3.01 obtained by the four-corner MTP for size 25×25.

Although it is impossible to know the exact values of the fractal dimensions of real-life images, the above comparisons show that, compared with the divisor-step algorithm, our proposed algorithms more likely obtain fractal dimensions within the theoretical range. In addition, these three algorithms are constructed from three different perspectives but can obtain similar mean of the

Table 3
The extremes, maximum (Max) and minimum (Min), and the ranges of the local fractal dimensions of the extracted IKONOS residential image for each of the 16 moving-kernel sizes (from 9×9 to 69×69) for algorithms I, II, III, and IV, corresponding to the divisor-step, modification of the eight-pixel, four-corner, the moving-average algorithm respectively.

Sizes	Algorithm I			Algorithm II			Algorithm III			Algorithm IV		
	Max	Min	Range	Max	Min	Range	Max	Min	Range	Max	Min	Range
9×9	4.09	1.62	2.47	3.81	1.67	2.14	3.81	1.67	2.14	3.58	1.74	1.83
13×13	3.65	1.80	1.85	3.41	1.83	1.58	3.61	1.82	1.79	3.27	1.97	1.31
17×17	3.42	1.72	1.70	3.50	1.76	1.74	3.41	1.99	1.42	3.13	2.07	1.06
21×21	3.08	1.93	1.15	3.21	2.06	1.15	3.21	2.04	1.17	3.04	2.11	0.92
25×25	3.04	1.99	1.05	2.97	2.16	0.81	3.01	2.17	0.84	2.94	2.13	0.80
29×29	3.07	1.96	1.11	2.99	2.09	0.89	2.95	2.22	0.73	2.87	2.19	0.68
33×33	3.01	1.96	1.05	2.88	2.19	0.69	2.89	2.22	0.67	2.79	2.23	0.57
37×37	2.95	2.13	0.82	2.86	2.24	0.62	2.89	2.25	0.63	2.76	2.25	0.51
41×41	2.89	2.07	0.82	2.81	2.26	0.55	2.84	2.28	0.56	2.75	2.28	0.47
45×45	2.94	1.97	0.96	2.85	2.24	0.61	2.80	2.30	0.50	2.74	2.30	0.44
49×49	2.97	2.17	0.80	2.88	2.24	0.64	2.78	2.31	0.46	2.72	2.33	0.40
53×53	2.91	2.12	0.80	2.85	2.29	0.56	2.76	2.24	0.52	2.70	2.32	0.38
57×57	2.85	2.20	0.65	2.84	2.28	0.57	2.77	2.27	0.50	2.69	2.33	0.37
61×61	2.87	2.30	0.56	2.86	2.25	0.61	2.77	2.33	0.45	2.69	2.34	0.35
65×65	2.84	2.22	0.62	2.80	2.27	0.52	2.81	2.33	0.49	2.68	2.35	0.33
69×69	2.83	2.22	0.62	2.82	2.25	0.57	2.77	2.33	0.45	2.67	2.35	0.32

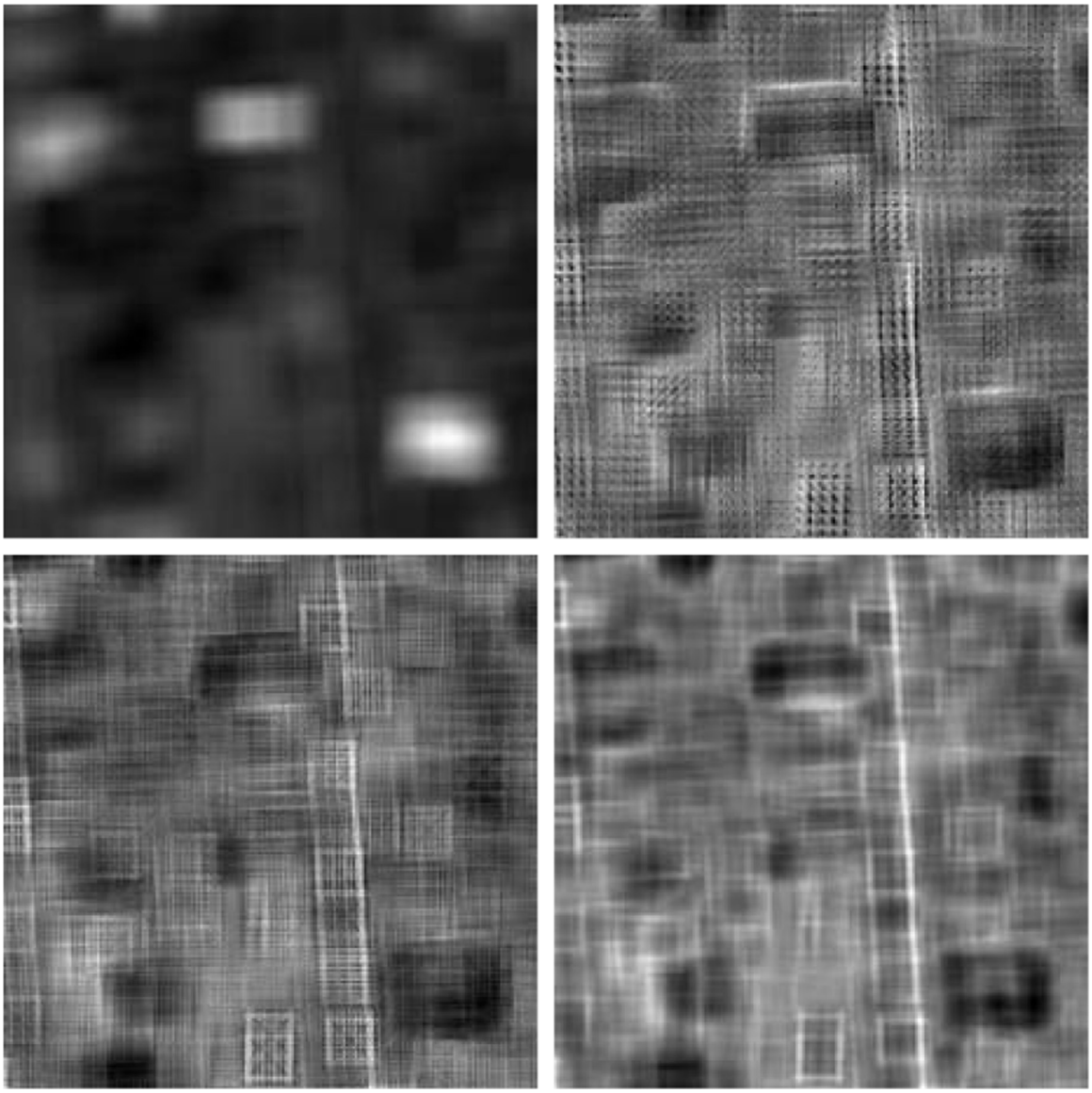

Fig. 12. Panels are arranged from the top left to the bottom right as (a)–(d). (a) Resampled image of the image in Fig. 10(a) using overlapping moving kernel with size 23×23. Panels (b)–(d) are fractal layers obtained for moving kernel with size 23×23 by the modified eight-pixel algorithm, four-corner algorithm and moving-average algorithm, respectively. The images displayed in all panels are rescaled to 0–255 for visual comparison.

local fractal dimensions, which is smaller than that obtained by the divisor-step algorithm. Thus, it is reasonable to conclude that although the four algorithms can lead to similar results for the simulated FBSs, the divisor-step algorithm more likely overestimates in real-life applications. Furthermore, the divisor-step algorithm is only applicable to images with specific size. In contrast to this algorithm, our proposed algorithms can break this limitation. To show this advantage, we apply the three proposed algorithms to the same extracted image shown in Fig. 10(a) with another moving-kernel of size 23×23. The resampled image and the obtained fractal layers are shown in Fig. 12. The obtained fractal layers can also reflect the textural features in panel (a).

With regard to the NTL example, Figs. 13 and 14 respectively show the results using the moving kernel with size 21×21 and 23×23. The performance of the divisor-step algorithm and the three proposed algorithms are generally similar to the IKONOS example shown in Figs. 10 and 12. However, the correspondence to the resampled image in panel (b) is not as good as that shown in the IKONOS example. Since the coastal line at the right-bottom corner can be well identified, the slightly worse performance in the NTL case should be due to the following two reasons: one of the reasons is that the NTL image has much less variation than the IKNONS image. Especially, the urban area with the saturation DN 63 and the totally dark area with DN 0 in panel (a) are actually the flat surfaces corresponding to the same fractal dimension 2. The other reason is that the NTL image consists of some clusters with different sizes. Some of these clusters are very small, even smaller than the size of the moving kernel. In this case, for each position, the moving kernel may cover both the NTL cluster and the dark area. Then the fractal dimension for each position as an index for this mixed status is not so much different from one another.

Based on the results of these two real-life examples, the texture feature extracted by the fractal analysis is largely from the variation of images, which can be intuitively understood as a kind of roughness. In this sense, we do not recommend the fractal analysis for the relative simple image, such as the NTL image with less variation.

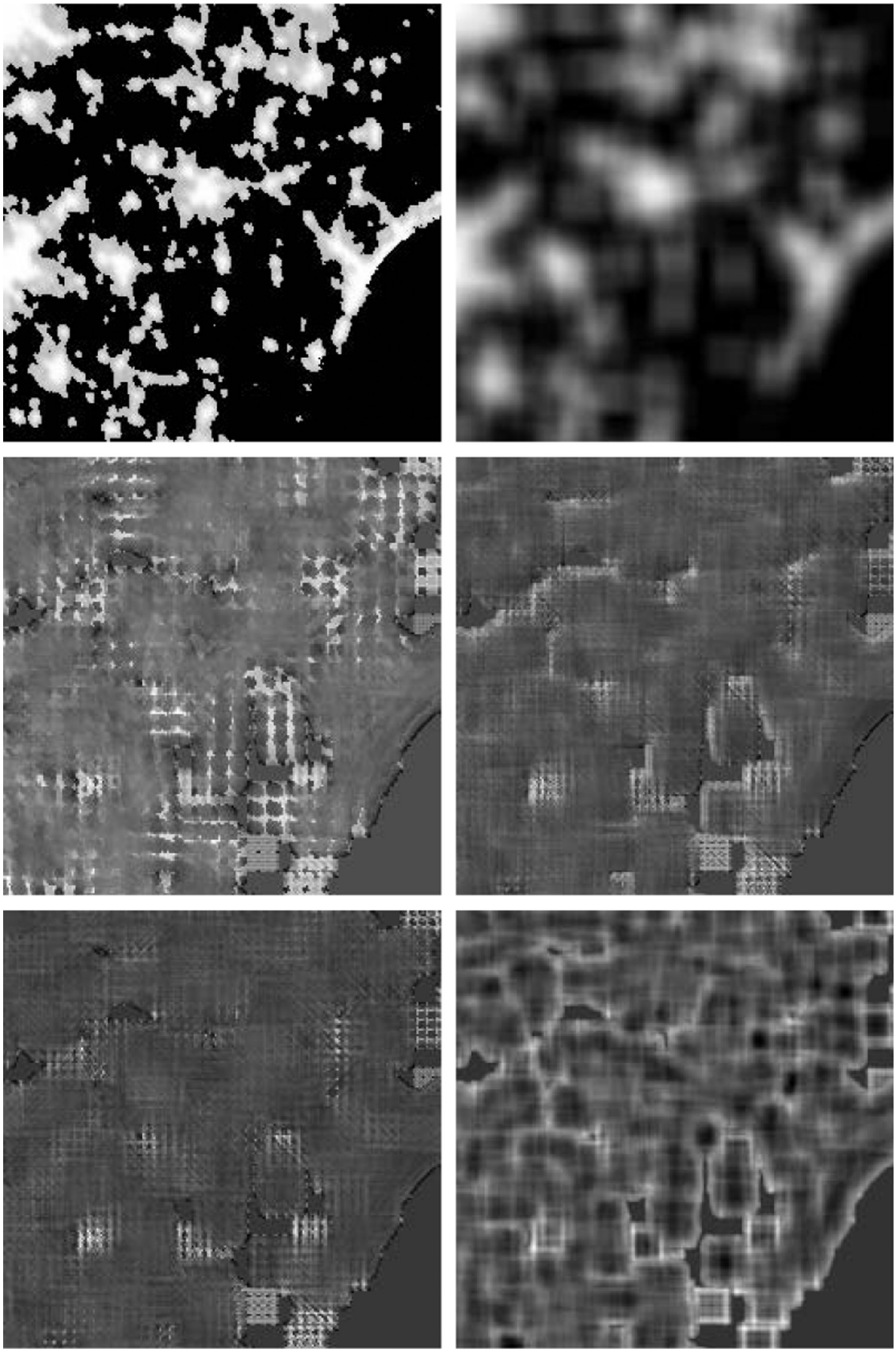

Fig. 13. Panels are arranged from the top left to the bottom right as (a)–(f). (a) The image extracted from an NTL image covering a southeastern part of the USA. (b) Re-sampled image of the image in panel (a) using overlapping moving kernel with size 21×21. Panels (c)–(f) are fractal layers obtained for moving kernel with size 21×21 by the divisor-step algorithm, the modified eight-pixel algorithm, the four-corner algorithm and the moving-average algorithm, respectively. The images displayed in all panels are rescaled to 0–255 for visual comparison.

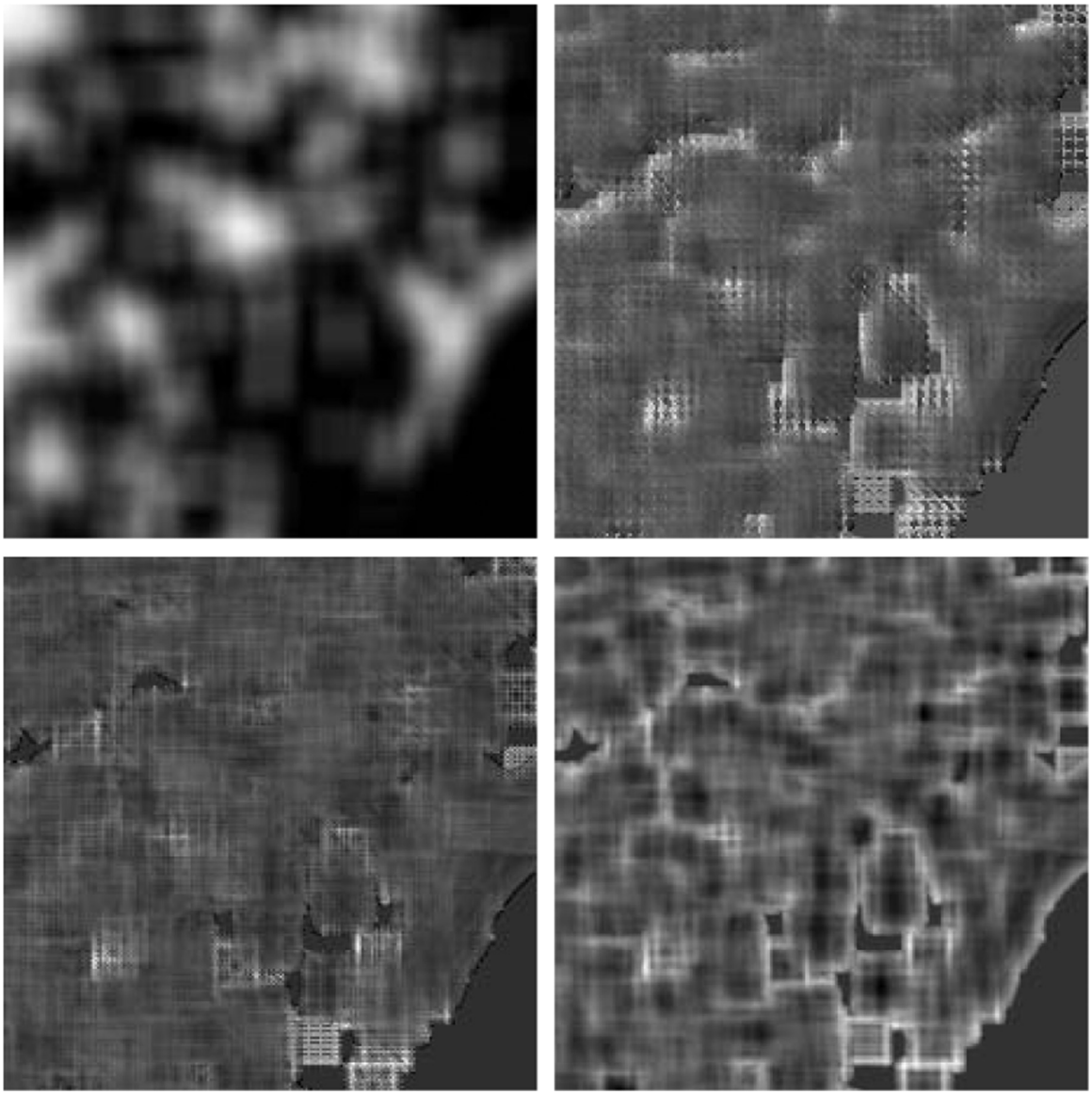

Fig. 14. Panels are arranged from the top left to the bottom right as (a)–(d). (a) Resampled image of the image in Fig. 13(a) using overlapping moving kernel with size 23×23. Panels (b)–(d) are fractal layers obtained for moving kernel with size 23×23 by the modified eight-pixel algorithm, four-corner algorithm and moving-average algorithm, respectively. The images displayed in all panels are rescaled to 0–255 for visual comparison.

5. Conclusions

Although claimed to be the most reliable method among the MTP, isarithm, variogram, probability, and variation method (Zhao, 2001; Lam et al., 2002; Zhou and Lam, 2005), the MTP has been shown to have much room for improvement from different perspectives (Sun, 2006; Ju and Lam, 2009a,b). To improve the MTP, we algorithmically investigate the MTP in this study and identify three factors affecting the estimation of fractal dimensions, namely (F1) the number of steps; (F2) the step sizes; and (F3) estimation accuracy of the facet areas of the triangular prisms. Existing algorithms usually focus on only one factor, such as (F2) in the divisor-step algorithm by Ju and Lam (2009a,b), and (F3) in the eight-pixel algorithm by Sun (2006). Taking into consideration all factors simultaneously, we propose three algorithms in the present study, namely the modification of the eight-pixel algorithm, the four-corner MTP and the moving-average MTP. It should be emphasized that the proposed algorithms are not limited by specific image size, which is required by the divisor-step algorithm.

Numerical experiments show that our algorithms are comparable to the divisor-step algorithm, but superior to the eight-pixel algorithm with respect to the mean of the computed fractal dimensions and the RMSE. All proposed algorithms obtain reliable results for moderate sizes for all selected fractal dimensions but become less accurate for smaller or larger sizes, especially when the fractal dimension is larger than 2.5. In the real-life application, our proposed algorithms and the divisor-step algorithm can all extract the basic textural features. In addition, it is found that the moving-average algorithm has the capacity to reduce the sensitivity of the MTP to the noise or extreme value of pixels. It is impossible to know exactly the actual value of the fractal dimension of real-life remotely-sensed images. However, the comparison of the mean values of the fractal dimensions shows that our algorithms obtain similar results while the divisor-step algorithm tends to obtain larger values. Considering that three algorithms are proposed from different perspectives, what we could conclude is that similarity of their results more likely estimate the real fractal dimensions. In addition, the divisor-step algorithm more likely gives the local fractal dimensions beyond the theoretical range. With regard to the selection of algorithms

for fractal analysis, especially in application to remotely sensed images, we recommend the four-corner MTP and the moving-average MTP, which can overcome the limitation of the divisor-step algorithm to specific moving-kernel sizes and can handle the incomplete coverage issue without making any specific assumption. In addition, the moving-average MTP is insensitive to noise or extreme values. By combining and comparing the results of both algorithms, we can evaluate the influence of extreme values of pixels and then have a complete profile of the analyzed images.

Despite the importance of using fractal dimension as an important index for quantifying the complexity and roughness of images, it is still difficult to give its specific meaning. Even for a non-ideal fractal image, the obtained fractal dimension reflects some texture information about it in average. It has been shown that the texture feature uncovered by the fractal analysis is basically from the roughness/variation of the image. However, finding out the specific meaning is one of the important tasks in future research.

Acknowledgments

This work was supported by the earmarked Grant CUHK444411 of the Hong Kong Research Grants Council and the Geographical Modeling and Geocomputation Program under the Focused Investment Scheme of The Chinese University of Hong Kong. The authors would like to thank Prof. Zu-Guo Yu for his valuable discussion and suggestion. We would like to thank the editor and two anonymous referees for their comments and suggestions in improving this paper.

Appendix A. Supplementary data

Supplementary data associated with this paper can be found in the online version at http://dx.doi.org/10.1016/j.cageo.2016.02.018.

References

Batty, M., Longley, P., 1994. Fractal Cities. Academic Press, New York.
Bretar, F., Arab-Sedze, M., Champion, J., Pierrot-Deseilligny, M., Heggy, E., Jacquemoud, S., 2013. An advanced photogrammetric method to measure surface roughness: application to volcanic terrains in the Piton de la Fournaise, Reunion Island. Remote Sens. Environ. 135, 1–11.
Ceccato, P., Gobrona, N., Flasseb, S., Pintya, B., Tarantola, S., 2002. Designing a spectral index to estimate vegetation water content from remote sensing data: Part 1: theoretical approach. Remote Sens. Environ. 82, 188–197.
Cheng, Q., 1999. The gliding box method for multifractal modeling. Comput. Geosci. 25, 1073–1079.
Cheng, Q., 2005. Multifractal modeling of eigenvalues and eigenvectors of 2-D maps. Math. Geol. 37, 915–927.
Cheng, Q., 2014. Generalized binomial multiplicative cascade processes and asymmetrical multifractal distributions. Nonlinear Process. Geophys. 21, 477–487.
Cheng, Q., Agterberg, F.P., 2009. Singularity analysis of ore-mineral and toxic trace elements in stream sediments. Comput. Geosci. 35, 234–244.
Clarke, K.C., 1986. Computation of the fractal dimension of topographic surfaces using the triangular prism surface area method. Comput. Geosci. 12, 713–722.
De Jong, S.M., Burrough, P.A., 1995. Fractals in physical geography. Photogrammet. Eng. Remote Sens. 61, 1041–1053.
Emerson, C.W., Lam, N.S.N., Quattrochi, D.A., 1999. Multi-Scale Fractal analysis of image texture and pattern. Photogrammet. Eng. Remote Sens. 65, 51–61.
Feder, J., 1988. Fractals. Plenum Press, New York.
Gao, J., Xia, Z.-G., 1996. Fractals in physical geography. Prog. Phys. Geogr. 20, 178–191.
Goodchild, M., Mark, D., 1987. The fractal nature of geographic phenomena. Ann. Assoc. Am. Geogr. 77, 265–278.
Hodgson, M.E., 1998. What size window for image classification? A cognitive perspective. Photogrammet. Eng. Remote Sens. 64, 797–807.
Jaggi, S., Quattrochi, D., Lam, N.S.-N., 1993. Implementation and operation of 3 fractal measurement algorithms for analysis of remote-sensing data. Comput. Geosci. 19, 745–767.
James, T.D., Carbonneau, P.E., Lane, S.N., 2007. Investigating the effects of DEM error in scaling analysis. Photogrammet. Eng. Remote Sens. 73, 67–78.
Jensen, J.R., 1986. Introductory Digital Image Processing. Prentice-Hall, Englewood Cliffs, NJ.
Jiao, L.M., Liu, Y.L., Li, H.L., 2012. Characterizing land-use classes in remote sensing imagery by shape metrics. ISPRS J. Photogrammet. Remote Sens. 72, 46–55.
Ju, W., Lam, N.S.-N., 2009a. An improved algorithm for computing local fractal dimension using the triangular prism method. Comput. Geosci. 35, 1224–1233.
Ju, W., Lam, N.S.-N., 2009b. An improved algorithm for computing local fractal dimension using the triangular prism method. Comput. Geosci. 35, 1224–1233.
Kauth, R.J., Thomas, G.S., 1976. The Tasseled Cap—a graphic description of the spectral-temporal development of agricultural crops as lakes by landsat. In: Proceedings of the Symposium on Machine Processing of Remotely Sensed Data, pp. 4B41–4B51.
Lam, N.S.-N., 2008. Methodologies for mapping land cover/land use and its change. In: Liang, S. (Ed.), Advances in Land Remote Sensing: System, Modeling, Inversion and Application. Springer, New York, pp. 341–367.
Lam, N.S.-N., De Cola, L., 1993. Fractals in Geography. Prentice-Hall, PTR.
Lam, N.S.-N., Qiu, H.-L., Quattrochi, D.A., Emerson, C.W., 2002. An evaluation of fractal methods for characterizing image complexity. Cartogr. Geogr. Inf. Sci. 29, 25–35.
Lam, N.S.-N., Quattrochi, D.A., 1992. On the issues of scale, resolution, and fractal analysis in the mapping sciences. Prof. Geogr. 44, 88–98.
Leung, Y., Fung, T., Mi, J.S., Wu, W.Z., 2013. A rough set approach to the discovery of classification rules in spatial data. Int. J. Geogr. Inf. Sci. 21, 1033–1058.
Liang, B., Weng, Q., Tong, X., 2013. An evaluation of fractal characteristics of urban landscape in Indianapolis, USA, using multi-sensor satellite images. Int. J. Remote Sens. 34, 804–823.
Lo, C.P., 1986. Applied Remote Sensing. Brunt Hill, Harrow.
Mandelbrot, B., 1982. The Fractal Geometry of Nature. W.H. Freeman, New York.
Mark, D.M., Aronson, P.B., 1984. Scale-dependent fractal dimensions of topographic surfaces: an empirical investigation with application in geomorphology and computer mapping. Math. Geol. 16, 671–683.
Melgani, F., Bruzzone, L., 2004. Classification of hyperspectral remote sensing images with support vector machines. IEEE Trans. Geosci. Remote Sens. 42, 1778–1790.
Myint, S.W., 2003. Fractal approaches in texture analysis and classification of remotely sensed data: comparisons with spatial autocorrelation techniques and simple descriptive statistics. Int. J. Remote Sens. 24, 1925–1947.
Munyati, C., 2004. Use of principal component analysis (PCA) of remote sensing images in wetland change detection on the Kafue Flats, Zambia. Geocarto Int. 19, 11–22.
Ollier, S., Chessel, D., Couteron, P., Pelissier, R., Thioulouse, J., 2003. Comparing and classifying one-dimensional spatial patterns: an application to laser altimeter profiles. Remote Sens. Environ. 85, 453–462.
Pentland, A.P., 1984. Fractal-based description of natural scenes. IEEE Trans. Pattern Anal. Mach. Intell. 6, 661–674.
Qiu, H.L., Lam, N.S.-N., Quattrochi, D., Gamon, J., 1999. Fractal characterization of hyperspectral imagery. Photogrammet. Eng. Remote Sens. 65, 63–71.
Quattrochi, D., Lam, N.S.-N., Qiu, H., Zhao, W., 1997. Image Characterization and Modeling System (ICAMS): a geographic information system for the characterization and modeling of multiscale remote sensing data. In: Quattrochi, D. A., Goodchild, M.F. (Eds.), Scale in Remote Sensing and GIS. CRC Press, LLC, FL, pp. 295–308.
Read, J.M., Lam, N.S.-N., 2002. Spatial methods for characterising land cover and detecting land-cover changes for the tropics. Int. J. Remote Sens. 23, 2457–2474.
Schertzer, D., Lovejoy, S., 1987. Physical modeling and analysis of rain and clouds by anisotropic scaling multiplicative processes. J. Geophys. Res. 92, 9693–9714.
Shelberg, M.C., Lam, N.S.-N., Moellering, H., 1983. Measuring the fractal dimension of surfaces. In: Proceedings of the Sixth International Symposium on Computer-Assisted Cartography (Auto-Carto 6), Ottawa, Ontario, Canada, pp. 319–328.
Shen, Y., Di, L., Yu, G., Wu, L., 2013. Correlation between corn progress stages and fractal dimension from MODIS-NDVI time series. IEEE Geosci. Remote Sens. Lett. 10, 1065–1069.
Silvetti, A.F., Delrieux, C.A., 2013. Quadratic self-correlation: an improved method for computing local fractal dimension in remote sensing imagery. Comput. Geosci. 60, 142–155.
Sun, W., 2006. Three new implementations of the triangular prism method for computing the fractal dimension of remote sensing images. Photogrammet. Eng. Remote Sens. 72, 373–382.
Sun, W., Xu, G., Gong, P., Liang, S., 2006. Fractal analysis of remotely sensed images: a review of methods and applications. Int. J. Remote Sens. 27, 4963–4990.
Townshend, J., Justice, C., Li, W., Gurney, C., McManus, J., 1991. Global land cover classification by remote sensing: present capabilities and future possibilities. Remote Sens. Environ. 35, 243–255.
Xia, Z.G., Clarke, K.C., 1997. Approaches to scaling of geo-spatial data. In: Quattrochi, D.A., Goodchild, M.F. (Eds.), Scale in Remote Sensing and GIS. CRC Press, LLC, F., pp. 309–360.
Xia, Y., Feng, D., Zhao, R., Zhang, Y., 2010. Multifractal signature estimation for textured image segmentation. Pattern Recognit. Lett. 31, 163–169.
Zhao, W., 2001. Multiscale Analysis for Characterization of Remotely Sensed Images (Ph.D. dissertation). Louisiana State University, Baton Rouge, LA, 239 p.
Zhou, G., Lam, N.S.-N., 2005. A comparison of fractal dimension estimators based on multiple surface generation algorithms. Comput. Geosci. 31, 1260–1269.
Zhu, J., Shi, J.C., Chu, H.F., Hu, J.W., Li, X.Z., Li, W., 2011. Remote sensing classification using fractal dimensions over a subtropical hilly region. Photogrammet. Eng. Remote Sens. 77, 65–74.